

Laser Structured Gas Diffusion Layers for Improved Water Transport and Fuel Cell Performance

Christoph Csoklich,[†] Hong Xu,[†] Federica Marone,[‡] Thomas J. Schmidt,^{†,¶} and Felix N. Büchi^{*,†}

[†]*Paul Scherrer Institut, Forschungsstrasse 111, 5232 Villigen, Switzerland*

[‡]*Swiss Light Source Paul Scherrer Institut, 5232 Villigen, Switzerland*

[¶]*Laboratory of Physical Chemistry, ETH Zürich, Vladimir-Prelog-Weg 1-5/10, 8093 Zürich, Switzerland*

E-mail: felix.buechi@psi.ch

Phone: +41 (0)56 310 24 11

Abstract

Polymer electrolyte fuel cells are promising energy converters for future green energy systems. For wide commercial use, still cost reductions by increasing the power density are required. Structurally optimized gas diffusion layer (GDL), allowing for cell operation at high current densities, with reduced mass transport losses, are an essential component for this development. Here we demonstrate that GDLs modified with perforations can improve water transport in the high current density regions and increase fuel cell performance. Laser perforation prior to GDL hydrophobization circumvents previously observed flooding problems and allow for stable operation. The advanced pattern connecting channel and land regions drains pores hence decreasing the liquid water

fraction, especially close to the GDL and catalyst layer interface. *Operando* dynamic X-Ray tomographic microscopy (XTM) is employed to understand water transport in the modified structure and the competition with random break-through of water clusters to the channel is analyzed. The detailed and time resolved insights allow for proposing guidelines for future advanced patterning geometries, suggesting denser perforations and methods to counteract the observed HFR increase. Furthermore, this approach can act as model system for next generation GDLs and lead to a more rational design of transport layers.

Keywords

polymer electrolyte fuel cell, gas diffusion layer, water management, operando X-ray tomographic microscopy

1 Introduction

Polymer electrolyte fuel cells (PEFCs) are a promising technology for clean and sustainable hydrogen to power conversion for both mobile and stationary applications.^{1,2} However, the high capital expenditure (CAPEX) of today’s fuel cell systems, driven mainly by the fuel cell material’s costs, hinder their wider use and market penetration.³ The New Energy and Industrial Development Organization of Japan (NEDO) has drawn an ambitious road map to tackle this challenges with one key message: the power density of fuel cell systems has to be doubled (from a 2010 baseline of 1.2 W cm^{-2}) until 2030 (exp. 2.5 W cm^{-2}) and tripled until 2040 (exp. 3.7 W cm^{-2}).^{4,5} This can only be achieved with advanced catalysts (increasing the operating voltage) and transport layer materials (allowing to reach high current densities), which are investigated in this work.⁶

Today’s transport layers consist of a GDL substrate coated with a micro-porous layer (MPL). The MPL is a nanoporous structure, comprised mainly of carbon nanoparticles and

a fluoropolymer binder also serving for wet-proofing.⁷ It provides smooth mechanical and electrical contact with the catalyst layer (CL) on one interface and discrete product water injection sites at the MPL/GDL interface. In recent years, significant improvements have been achieved with the understanding and development of advanced MPLs structures.^{8,9} However, also the GDL plays a key role for PEFC operation and water management. It connects MPL and/or CL to the feed gas channels and has to fulfill several transport requirements in its pore and solid phases. Electrons and heat are conducted in the solid, reactant gases and water in the pore space. The GDL needs to distribute the reactant gases homogeneously from the channels to the catalyst layer and acts as a spring in the stack assembly, which is important for an even pressure distribution in each cell.^{10,11}

Conventional GDLs are dry or wet layered paper-like sheets of stacked or entangled carbon fibers with a thickness in the range of about 150 μm to 220 μm . As a consequence of this production process, GDLs inherently have a stochastic pore network that can be described with bulk descriptors such as porosity and pore size distribution, that are subject to strong local variations.^{12,13} The random pore and throat network causes the reactants and products to diffuse and move on torturous paths through the structure. Even though the materials are usually wet-proofed, their structure impacts especially liquid product water transport.^{14,15} In the capillary transport regime (the main one in GDLs), the distribution of water will follow the path of least resistance.¹⁶ This resistance is determined by the breakthrough pressure necessary for the water front to break through a narrow throat. It is a function of the liquid's surface tension γ , the contact angle at the solid surface σ and the throat radius r that can be put into relation with the Young-Laplace equation.¹⁷ A random distribution of narrow throats can lead therefore to significant (in-plane) water saturation of the GDL, before break-through to the channels is reached, when the capillary pressure drops and water is released into the channels to drain the structure.^{18,19} Additionally, water condensation and accumulation occurs below the flow field ribs, as this heat sink is slightly colder than the surrounding structure.²⁰ The liquid water in the GDL's pore space blocks and elongates

reactant gas pathways, increasing especially the oxygen transport resistance on the cathode side.²¹ At high current densities, this limits mass transport to the catalyst and is one of the main challenges on the way to higher power density fuel cells. Key for enhanced performance is to increase the effective diffusivity and to release liquid product water through the most direct way from the structure. Results from XTM show, that the water release processes are strongly dependent on the local orientation and fiber surface properties.^{22,23} Together with the consideration of water accumulation below flow field ribs, which originates from the conventional channel and rib flow field geometry, this leads to the concept of structured materials for improved water transport.

Two main approaches of structuring the GDL have been investigated in the last decade: a chemical (changing the contact angle σ) and a physical (changing the pore radius r) modification of the pathway. On the chemical route, local variation of the wet proofing was studied by Koresawa et al. or Forner-Cuenca et al. .²⁴⁻²⁶ Local, physical methods included mainly perforations of the GDL and/or MPL by drilling, punching or laser irradiation.^{9,27-30} The approach with laser perforations offers a simple and durable solution that creates direct water pathways through parts or the whole GDL. In these perforations, due to the enlarged throat diameter, the breakthrough pressure is decreased and water is more likely to invade there. Performance improvements have been shown in previous studies, but also detrimental effects of the perforated GDLs under wet conditions were observed. This was attributed to the additional removal of the wet-proofing agent in the vicinity of the perforation by the laser treatment and observed in (*operando*) X-Ray and neutron imaging.^{29,31} However, a more detailed description of the water transport in the modified GDLs as well as a conclusive separation of wet proofing and structural effects in the GDL is missing.

In this study, we investigate the water transport in laser perforated GDLs using sub-second *operando* XTM for characterization of the liquid water dynamics. An adapted wet-proofing and perforation procedure is presented that not only prevents the formation of hydrophilic areas after laser perforation, but also connects channel and rib areas of the GDL

in the form of perforated slits. The model system used is a commercial Toray carbon paper (Toray TGP-H-060), perforated and wet-proofed in house.

With the *operando* imaging technique, water transport in GDL perforations is analyzed and the observations allow for proposing guidelines for future advanced patterning geometries. Furthermore, perforated GDLs can act as model system for a more rational design of transport layers.

2 Results

As base material for this study Toray carbon paper (TGP-H-060) is used, that is laser perforated with a $50\text{ }\mu\text{m}\times 1\text{ mm}$ line pattern (*P5:100*, 2.6% perforated area) and wet-proofed with FEP (to 20 %wt) in-house. Both unperforated (referred to as *T60*) and perforated (*T60-P5:100*) samples were assembled in small, differential fuel cells for electrochemical analysis ($5\text{ cm}^2 A_{act}$) and for tomographic imaging ($0.16\text{ cm}^2 A_{act}$). The water distribution was observed by fast imaging of the structure during polarization curves under humidity saturated conditions. Time-resolved water dynamics for the modified GDL at constant water production rate are studied following a current jump.

2.1 Electrochemical Performance

Determining the electrochemical performance in small, differential cells enables a straightforward approach to characterize materials and operating conditions without complex down the channel gradients. The used active area of 5 cm^2 is still large enough to minimize boundary effects, while guaranteeing a large number of perforations to be averaged across the GDL area. Figure 1a shows the polarization curves of the *T60* and *T60-P5:100* samples at conditions of $80\text{ }^\circ\text{C}$, 150 kPa and feed gas humidities of 80%/60% and 80%/100% (A/C). The high relative humidity case was chosen to mimic cell conditions during high power operations in a stack, where water accumulates down the channel.

At dry feed gas conditions (60% RH at the cathode), native and perforated GDLs have a comparable performance. Only the high frequency resistance (HFR) of the perforated material is slightly increased by 15%. We assume that this is due to slightly increased membrane drying due to the locally increased diffusivity in the perforation and related loss of water from the membrane. Under "wet" feed gas conditions (100% RH at cathode), *T60-P5:100* shows however an increased performance as shown in Figure 1a. For both GDL materials the characteristic mass transport related voltage drop is observed, though the onset occurs at different current densities. The current density difference at 0.6 V is 140 mA cm^{-2} (+10%), and the maximum achieved current density for *T60-P5:100* is 250 mA cm^{-2} higher than for *T60*.

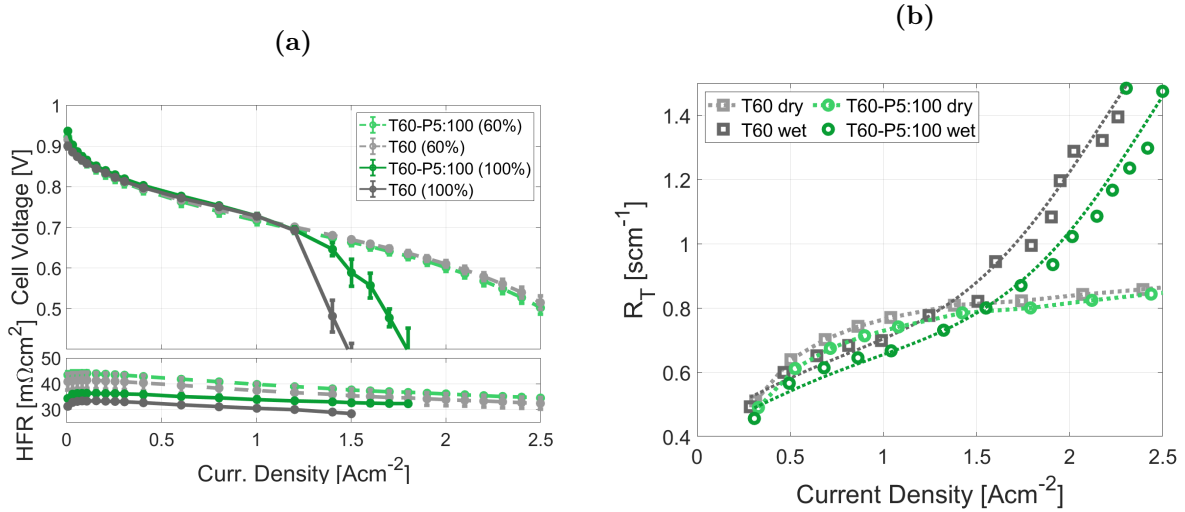


Figure 1: a) Polarization curves for ($5 \text{ cm}^2 A_{act}$) cells with *T60* in gray, and *T60-P5:100* in green and high frequency resistance (HFR) at a cell temperature of 80°C , gas pressures of 150 kPa for two relative gas humidities of 80/60% and 80/100 % (A/C); b) oxygen transport resistance as a function of the limiting current at a cell temperature of 80°C , pressure of 150 kPa and gas humidities of 60%/60% ("dry") and 80%/95% ("wet") (A/C).

The improved performance under "wet" conditions is mirrored in the results of the oxygen transport resistance R_T , presented in Figure 1b. Limiting current measurements to calculate R_T were conducted at similar "dry" and "wet" operating conditions, following the procedures described in literature.^{8,32} In "dry" gas conditions (RH of 60% on both sides), the difference in R_T is only around 6% for current densities up to 2.5 A cm^{-2} , and thus in the order of the

measurement uncertainty (estimated to $\approx 3\%$).

For the "wet" conditions, (95% on the cathode side, to avoid massive water condensation and blocking gas channels), already at low current densities (corresponding to low oxygen concentrations), a significant difference of around 10% in R_T is observed between the two materials. At about 1.5 A cm^{-2} , the oxygen transport resistance sharply increases for the base material, but slightly later and less steep for *T60-P5:100*. Therefore, ΔR_T grows to 15% at 21% O_2 concentration (corresponding to $\approx 2.3 \text{ A cm}^{-2}$ in Figure 1b).

The later onset in the transport resistance ($\approx 2 \text{ A cm}^{-2}$ as compared to $\approx 1.3 \text{ A cm}^{-2}$ for the polarization curve) is expected to be caused by the slightly lower cathode gas humidity.

2.2 Image-based Analysis

2.2.1 Steady-state Water Saturation Under Varying Load

The setup used for *operando* XTM experiments provided a voxel size of $2.75 \mu\text{m}$ and a scan time of 0.25 s, ideal for capturing fast water dynamics in the GDL pore space. Figure 2a shows a cross-section through the tomography cells (*T60* on top, *T60-P5:100* at the bottom). The fibers were sufficiently resolved and decent contrast between the solid and void was achieved, allowing for extracting the GDL's water saturation at varying load set-points. The cells showed a similar operating behaviour (compared to the 5 cm^2 cell) with similar performance in dry conditions and substantial differences in both voltage and maximum current density (at 330 mV) for the perforated GDL, as is shown in Figure S1.

The property of main interest is the water saturation in the GDL, presented in Figure 2b. However, the average *total* water saturation in the cathode GDLs shows no difference for the two materials. Except for the difference at $j < 0.2 \text{ A cm}^{-2}$ (caused by insufficient initial drying of *T60-P5:100*), the two materials show a comparable total saturation vs. current density behavior and both materials show a final saturation of around 40% . It should be however noted, that *T60-P5:100* reaches about 10% higher current densities. At first glance, the better performance of *T60-P5:100* (see Figure 1a) at a similar water saturation seems

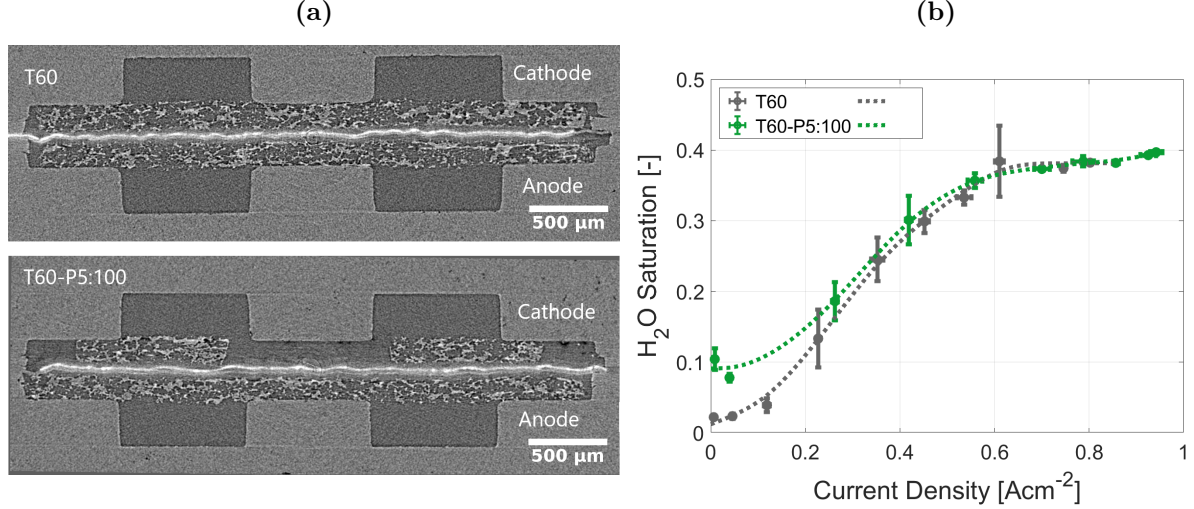


Figure 2: a) Vertical tomography slices ($0.16 \text{ cm}^2 A_{act}$) cells with *T60* (top) and *T60-P5:100* (bottom cf. perforations in the GDL); b) total water saturation in the cathode GDLs for both materials (gray: *T60*, green: *T60-P5:100*) as a function of the current density during the polarization curve (error bars in y-direction indicate the standard deviation as for each set voltage point three scans were recorded, error bars in x-direction indicate the standard deviation of the current density during these three scans).

inconsistent, but a more detailed analysis of the spatially resolved water saturation clears up this contradiction.

Figure 3 shows the 2D water saturation in the cathode GDL in the along-the-channel direction as a projection across the channel (x-axis shows the distance from cell entry to cell exit). Two descriptive current densities at approximately 0.45 A cm^{-2} and 0.75 A cm^{-2} have been chosen. In the top image, showing the water saturation at 0.45 A cm^{-2} , *T60* shows small areas of high saturation close to the MPL/GDL interface (thus close to the CL), a comparably dry center and some condensation below the ribs. On the right side, the line pattern of *T60-P5:100* is well visible: in distinct distances of 1 mm locally soaring water saturations are reached. These saturation maxima are confined to a very narrow space, i.e. only the slit itself. However, some areas of increased saturation appear also away from the slits, leading to a low to medium saturation (10 to 40%), present all across the observed volume. These effects increase the water saturation in the GDL center of *T60-P5:100*, but redistribute the water and prevent local wet spots, as seen for *T60*.

The higher current density water distribution at 0.75 A cm^{-2} shows an even clearer pic-

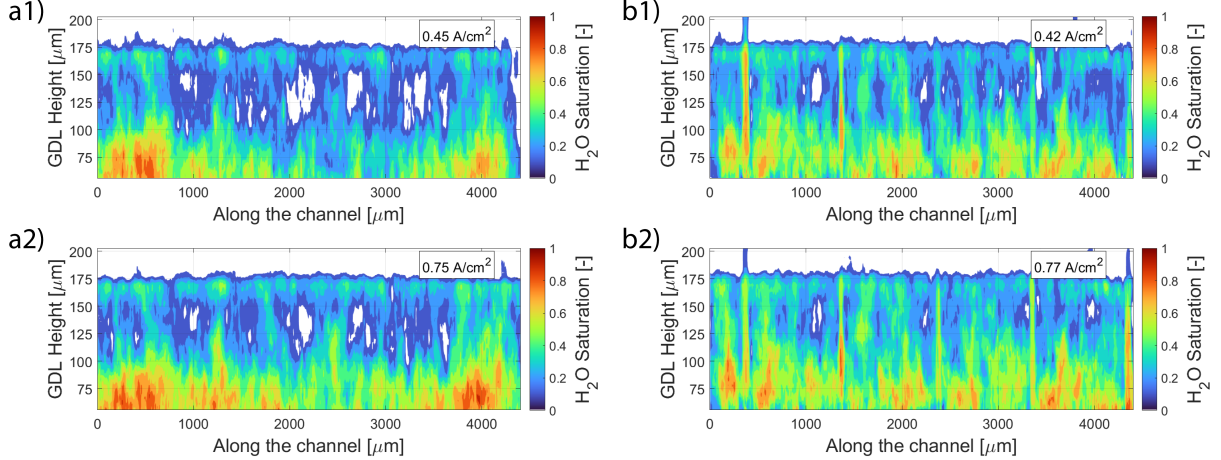


Figure 3: 2D water saturation S_w in the along-the-channel direction (x-axis shows channel length from cell entry to exit) in the cathode GDL of *T60* (a1-a2), and *T60-P5:100* (b1-b2) at two selected current densities (1, 2) of the polarization curve (1: 0.45 A cm^{-2} and 2: 0.75 A cm^{-2}).

ture. For the perforated sample, the saturation in the perforations further increases. Apart from the slits, two regions show above average saturation: at the GDL top (i.e. below the ribs, 55 to 70%, as can be seen in Figure S5), and close to the CL (40 to 80%). However, for *T60*, these regions are much more saturated, reaching there liquid water contents of 50 to 90% over large areas (cf. Figure SF). Close to the CL, the conventional GDL shows a very high water saturation along the channel. This flooding behaviour close to the MPL/GDL interface is detrimental for the gas supply. The effect is also quantified in Figure S4b and results in a by 20% reduced saturation at 0.8 A cm^{-2} for *T60-P5:100*.

Thus, two main observations can be summarized: first, the high saturation in the perforations and the lower saturation close to the CL indicate that product water is indeed transported through the slits away to the channel. However, the slightly increased saturation in the GDL center suggests, that the slits are not draining themselves but are accumulating water. Therefore, they are rather redistributing than draining the water (cf. Figure 2b). Overall the perforated GDL shows still a favourable water distribution allowing for higher current density operation than the standard material.

2.2.2 Dynamic Water Paths Development for a Perforated GDL

To shed more light into the water transport mechanism, the dynamics of water path evolution when starting from a dry GDL are analyzed for the perforated material *T60-P5:100* by fast imaging. An overview of the overall saturation development is given in Figure S6.

As observed above and hypothesized in literature, the perforations should act as direct water transport channels. Only water clusters connected to a slit can benefit from these regular drainage points. Water clusters unconnected to the perforations rely on the stochastic pore network and can thus spread far in in-plane directions. Therefore, a high water connectivity is crucial to drain the surrounding GDL areas with high water saturation.

Figure 4 shows a top view onto the GDL area. In gray, a projection of the GDL structure is shown, to show the location of the slits as well as the stochastic variation of the local porosity in the carbon GDL. In the top row of Figure 4, three snapshots of the water saturation at different time steps are presented (41 s, 102 s and 1502 s). Water connected to a slit and therefore easily draining to a channel is labeled in yellow, water not connected to the slits is shown in blue color. The turquoise color denotes both connected and unconnected water superposed in the projection.

It can be seen, that already after 41 s of operation liquid water appears in regions below the ribs. Furthermore, the slits start to fill. In this snapshot, just some small water clusters are connected to the perforations ($\approx 10\%$). However, after 102 s with increasing saturation more clusters are directly connected to the slits ($\approx 40\%$). Then, after 25 min of operation, the final water pattern is established: water is now present in all parts of the GDL, and the slight majority of the water is connected with a perforation ($\approx 50\text{-}60\%$).

In the lower three graphs of Figure 4, the history of the water clusters is included in the analysis: every water cluster once connected to a slit is labeled as connected. The hereby created connectivity map shows all GDL areas that have connected to the slits in the observed time span and thus highlights isolated spots, where water rather emerges to the channel directly than draining through a perforation. After 102 s (bottom center image)

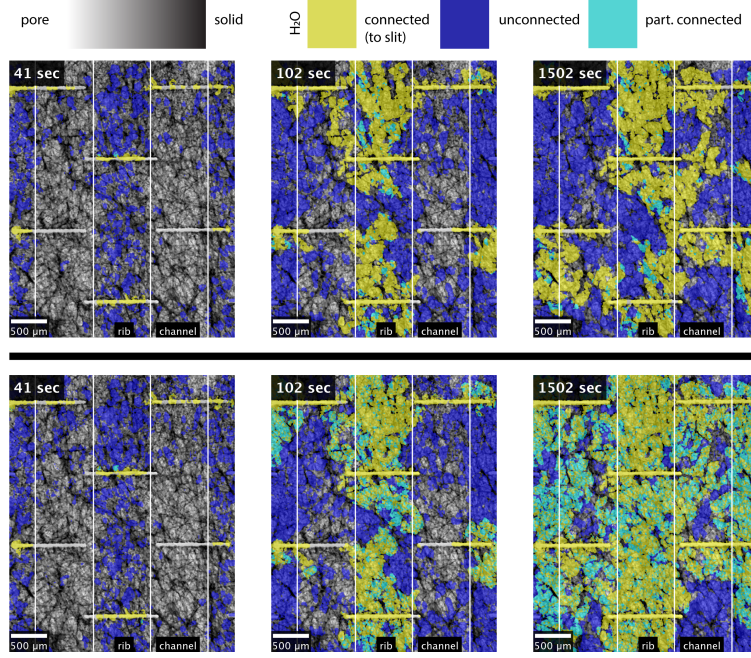


Figure 4: 2D Connectivity projection (along the GDL height) of water clusters in the cathode GDL of *T60-P5:100* GDL at three time-steps (41s, 102s and 1502s) at constant water production (constant current). The local porosity and fiber structure is shown in gray scale values; the water clusters connected to a slit in yellow, the unconnected clusters in blue, and areas with both types of clusters on top of each other in the projection in turquoise. The top row shows the current water saturation and cluster connectivity, the bottom row, previously connected clusters are also labelled as connected.

most of the water clusters below the central rib have already been connected to a perforation. However a substantial amount of unconnected water clusters form below the channels and the edges. The last time step (1502 s, bottom right image) shows that the majority of the pore space below the ribs is connected (and therefore drained), whereas the regions below the channel are only partly connected (indicated in turquoise, where connected and unconnected clusters overlap in the projection). This suggests that the perforations are capable of draining a significant fraction of product water in the rib area, but under the channels stochastic break through points, away from the slits exist. The qualitative results of Figure 4 are quantified below and are discussed in more detail later on.

Quantification of the connectivity and drainage efficiency is difficult to capture in a single metric. Therefore, three metrics have been evaluated. First, the total water saturation, S_w for water content quantification. Second, the ratio of water connected (to a perforation), termed here C_W to account for the drainage efficiency of the perforations. And third, the stretch of the connected water clusters into the observed volume was calculated. This ratio R_V , shows how far the connected clusters reach for a perforation, or if they emerge through the GDL surface somewhere else. All metrics were calculated for the entire cathode GDL as well as for an area/volume around each slit individually (area/volume definition around slits see Figure S7).

Results for the connectivity analysis are given in Figure 5. In Figure 5a the time evolution of the water saturation S_w (light blue line) shows that after around 30 s water starts to accumulate in the GDL until after about 300 s, a steady average saturation S_w of about 47% is reached. At the same time, the connectivity of water clusters to the perforations (C_W) increases from an initial state (a small amount of liquid water was already present in one perforation at the beginning) to a connectivity of 40 - 60%. The observed fluctuations in connectivity indicate drainage and re-saturation events. Unconnected water clusters grow either in-plane until they reach a perforation (increasing thereby C_W) or in through-plane direction until they reach the GDL's surface and form a break through outside the perforations.

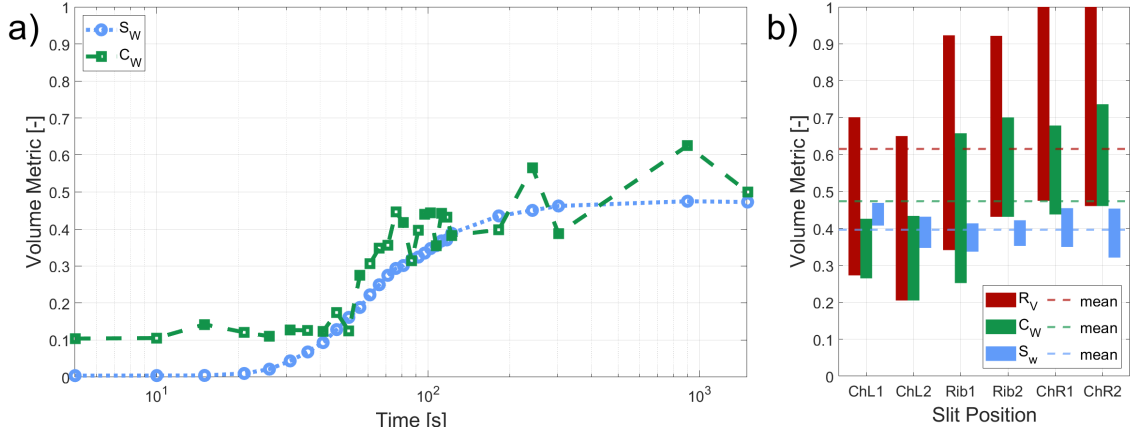


Figure 5: a) Time evolution of the water saturation S_w (light blue) and connectivity ratio C_W (green) for the entire GDL area as shown in Figure S7; b) min/max ranges of S_w , C_W and R_V during the last five scans of the steady state operation for each slit; the dashed lines indicate the mean value of the respective metrics.

For the connectivity analysis for single slits, volumes of about $2000 \times 990 \mu\text{m}^2$ around each slit were considered (definition see Figure S7). To illustrate the water dynamics at each slit (caused by saturation, drainage, snap off, etc.), the three metrics were calculated for the last five scans in the steady state phase (180 - 1502 s) (cf. Figure 5a). Figure 5b shows the span of each metric as colored bars, stretching from the minimum to the maximum value for each slit during the five observed scans. The mean values for each metric over all six slits are plotted with dashed lines.

The min/max of the volume reach R_V for the connected water varies about 60% of the observed GDL volume, indicating the dynamics of the water in the GDL. At the maximum, i.e. before a snap off event, the connected volume rises to 75% and higher. For slits ChR1 and ChR2, even the farthest regions of the observed volume were connected ($R_V \approx 100\%$) temporarily. This metric alone would therefore indicate, that the spacing of the slits is about sufficiently close for the Toray material. The average saturation S_w of 40 to 50% for each of the slit areas coincides well with the averaged value for the full GDL.

Also the connectivity of the water clusters in the slit areas shows similar values (around 50%) as the GDL average. However, this rather low connectivity seems to be in contradiction

to the high connected volume ratios around each perforation. It means that still a significant amount of water (30% in the best cases) is not connected. Inside the volumes spanned by the connected water, other clusters are prevented from connecting by the local pore geometry. Most likely this is by narrow throats present in the stochastic pore network, preventing long-range connectivity for all clusters. Therefore, break-through points (i.e. in anisotropic pores with large throats to the channel and small throats to the connected water) form outside the perforations, thus explaining the connectivity of water clusters to the slits of 50%. This effect of long stretched water clusters and stochastic break-through events is closer analyzed in the following.

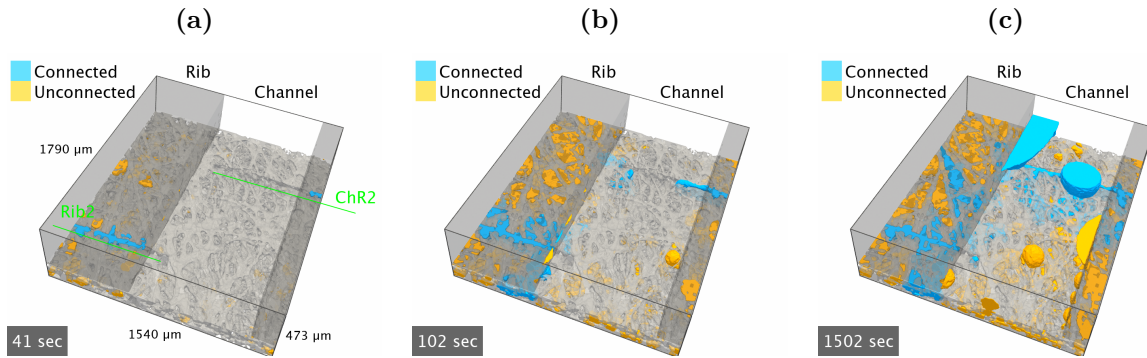


Figure 6: 3D renderings of cut-out area with two perforations, showing a time series of the evolution of water clusters and drainage events from the GDL to the channel. In light blue, clusters connected to slits and drainage events through perforations, in orange the remaining water clusters.

In Figure 6 the slits *ChR2* and *Rib2* (cf. Figure S7) are shown at the three time steps. This small focus is representative for water dynamics observed also at the other perforations. These renderings help to understand the competition between water drainage in perforations and the draining through stochastic pores. In light blue, water clusters connected to one of the two perforations are shown, the orange colored water denotes the clusters not connected to a slit, considered "stochastically" distributed clusters. Slit *Rib2* is located at the bottom left below the rib and slit *ChR2* at the top right of the volume. At early times (cf. Figure 6a after 41 s), water reaches and fills the perforation and is transported to the channel, while the area below the channel remains dry. After longer operation (102 s, Figure 6b), areas below the rib have reached high saturation, but clusters are still unconnected to the perforation.

In steady state (Figure 6c), connections to the perforation are established, and significant parts below the rib have connected and release water into the channel through the slits.

However, in both, Figures 6b and c water droplets (orange) are emerging into the channel away from the slits. This is, because non-connected clusters are intermixed with connected ones in the range of few 100 μm . Under steady state conditions (after 300 s) about 60% of water release droplets occur localized at the perforations, while the rest occurs stochastically through the GDL between the slits. The development with time is shown in Figure S8. These stochastic contributions of water drainage show that the stochastic nature of the pore network inhibits the complete connection to a perforation on the pore-level scale. This means that for complete drainage through slits, the perforations would need to be spaced somewhat narrower (for this GDL material).

A second effect responsible for this incomplete drainage process may be higher hydrophobicity in the vicinity of the perforations, as indicated by a higher fluorine signal, shown in Figure 7). Even though the morphology of the fibers close to the edge is not significantly changed by the laser treatment, this FEP accumulation near the slits may be caused by thermal modification of the fibre surface or higher solvent evaporation during the coating process near the perforations. The higher local FEP content may counteract the local decrease of break-through pressure in the large pore size slits and thus reduce the cluster connections to the slits. A more even distribution of the wet-proofing will be desirable in the further development of perforated GDL materials.

3 Discussion

In previous works laser perforations for optimizing the water management in GDLs were introduced into the base materials after hydrophobization, which rendered the perforations hydrophilic and thus the GDLs tended to flood.^{29,31} Contrary to this, in the present study perforations are also hydrophobic (hydrophobization after perforation) and the GDLs show

stable operating behavior from dry to wet conditions (cf. Figure 1).

Under wet feed gas conditions (100% RH at cathode), *T60-P5:100* shows an improved performance compared to the base material *T60* as shown in Figure 1a. The current density difference at 0.6 V is 140 mA cm^{-2} (+10%). This corroborates with the observed difference in oxygen transport resistance, that between the two materials (R_T at 2 A cm^{-2} in wet conditions is reduced by 13%).

While the *total* water saturation in the two structures is similar with about 40% at high current densities (cf. Figure 2b), the difference in performance is based on *spatially* different water saturation distributions (cf. Figure 3) that induce a water transport away from the GDL/MPL interface which strongly impacts the effective diffusivity of oxygen towards the catalyst layer.

At steady state water saturation (i.e. after 100 s), a water connectivity between 40% (where droplets are formed, snap off, and clusters are left unconnected) and 60% (prior to snap off events) is reached. However, the slits are not draining all product water, as is visible from Figure 6, where some unconnected droplets break through the GDL.

This leads to the following understanding of the impact of the perforation geometry: first, for draining all water through the slits, these may need to be spaced narrower to also drain the stretches of unconnected clusters, visible in Figure 4 in particular under the ribs. Secondly, the slit diameter might need to be slightly increased. The chosen value of $50 \mu\text{m}$ is likely too close to the mean pore size of the Toray base material of around $30 \mu\text{m}$ ^{33,34} so water tends to break through the larger stochastic pores to the channel. Increasing the total perforation area however, needs to be carefully considered. As seen in Figure 1a, in particular under dry conditions the HFR tends to increase with perforations, possibly due to membrane drying. The last design property of interest is the perforation length. Here, a general conclusion is difficult to draw, in addition to the above considerations. The time evolution data shows how the slits slowly fill below the rib until the channel is reached and droplets are formed. This indicates, that the selected length with 1 mm is well suited for

the rib width of 0.8 mm. Modern flow field designs with smaller ribs would therefore be sufficiently drained with slits of half the length. If the GDL can be placed accurately with respect to the flow field, even shorter perforations just connecting the rib/channel interface could be an option. This might also be a suitable perforation geometry for more dense slits, to prevent large in-plane water clusters. In combination with the specific pore size and pore geometry of the underlying base material, the balance of the three geometry parameters will determine the maximum potential for fuel cell performance increase by (laser) perforations.

4 Conclusion and Outlook

Development and evolution of all fuel cell's components is required for increasing power density in hydrogen fuel cells. Under a large range of operating conditions water management and transport from CL to gas channel will remain a critical hurdle to be overcome. In the presented research it is shown, that for the GDL structure a transition from fully stochastic pore networks to a more deterministic GDL structure can increase the cell performance. The laser-structuring method is considered a cheap and fast modification technique, common in a multitude of industrial processes from CD writing to steel cutting.³⁵

Under wet conditions, using laser perforated GDLs with hydrophobic slits, the power density at 0.6 V was increased by 15% and a more stable operating behavior was observed, with the oxygen transport resistance reduced by 13%.

Operando X-ray imaging shows that while the total saturation in the perforated and unmodified GDLs are comparable, the difference in performance stems from the local water distribution. The saturation in the perforated GDL shows about a 10% lower values near the GDL/MPL interface, resulting in improved oxygen transport towards the catalyst layer. To efficiently drain through the perforations, water clusters need to be connected to the slits. However, still a fraction of water clusters was observed to be unconnected to the perforations, causing them to grow in-plane or break through the GDL stochastically away from the slits.

This observation gives room for further geometry optimizations of the GDL materials.

Future adaptations of the perforation pattern can include denser spacing (less in-plane transport), larger slit diameters (further reduction in required break-through pressure and transition to bi-modal pore size distribution). Denser or larger perforations could however have drawbacks with respect to electrical resistance of the GDL and potentially increased membrane drying under dry conditions and so for further optimization all trade-offs must be carefully analyzed.

5 Experimental

5.1 Materials and Sample Preparation

Toray 60 (TGP-H-060, Alfa-Aesar/Torayca, JP) untreated carbon paper was used as base material (abbreviated as *T60*). A line pattern was burned through the entire thickness of the GDL with an engraving infrared laser (Trumpf Vector Mark, Nd:YAG, 1064 nm), as can be seen in Figure 1a (the details of the pattern parameters are given in Table 1.

Table 1: GDL sample and perforation details.

CELL-ID	GDL	mod.	width [μm]	length [μm]	spacing [mm]	perf. area [%]	porosity [-]
T60	TGP-H-060	none	-	-	-	-	0.49
T60-P5:100	TGP-H-060	line	50	1000	1x1	2.59	0.48

After the patterning step, GDLs were wet-proofed in-house with fluorinated ethylene propylene (FEP) in a dip-coating procedure following Forner-Cuenca et al. .²⁵ Pristine samples were cleaned with acetone, dried in a vacuum oven at 30 °C for 10 min and then immersed into a solution of 12.7% FEP in water (Evoqua Ultra Clear, 18.2 M Ω cm, Teflon™ FEPD 121, Chemours) for 30 s of each side. Afterwards, the GDLs were gently shaken to disperse the solution further and get rid of excess liquid in and on the structure for another minute. The samples were then dried in a vacuum oven (1: 30 °C, 1 °C min⁻¹, 2: 70 °C, 0.5 °C min⁻¹,

3: hold for 60 min, all at a chamber pressure of 10 mbar) and cooled down overnight. The last sintering step was performed in a muffle furnace at 280 °C (1: 260 °C, 4.5 °C min⁻¹, 2: hold for 10 min, 3: 280 °C, 1 °C min⁻¹, 4: hold for 30 min, 5: cool down overnight).

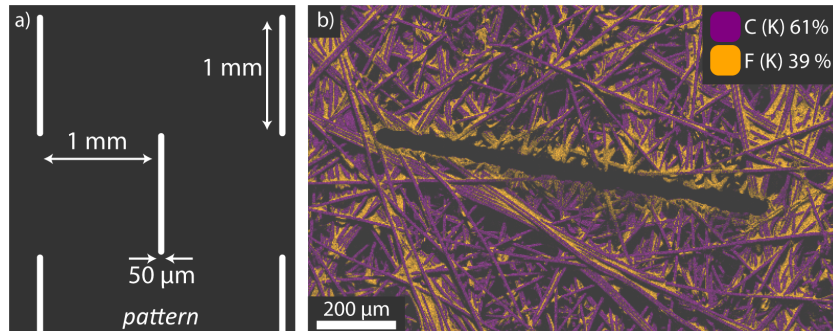


Figure 7: a) Schematic of the pattern geometry of 1 mm long and 50 μm wide slits and a spacing of 1 mm x 1 mm; b) EDX-mapping overlaying an SEM image showing the vicinity of a perforation after the wet-proofing step (K-edge signals for C in purple and F in orange).

Self-standing MPLs were prepared following the procedure described by Simon et al. .³⁶ Due to the lack of a planetary mixer, the slurries were mixed in a glass container under low pressure from a vacuum ejector on a magnetic stirring plate for around 1.5 h. Afterwards, the slurry was dispersed with a doctor blade across a glass plane (knife height above plane set to 300 μm). The thin films were dried at room temperature (covered, in a fume hood), until they could be peeled off the glass with a blade. The films were carefully placed on aluminium foil containers and then sintered with the same protocol used by Simon et al. .³⁶ The prepared MPL had a thickness of 35 μm.

5.2 Differential Cell Assembly and Testing

The described materials were used in a differential fuel cell with an active area of 5 cm². The same GDLs (plain or perforated) were used on both anode and cathode side for the respective cells. Gaskets (PTFE and FEP) with an overall thickness of 175 μm were chosen to reach a GDL compression of about 15%, when assuming a compression of the gaskets of 7%.⁸ As catalyst coated membrane (CCM) a fully catalyzed Gore Primea® (A510.1/M815.15/C510.4) membrane was used. The MEA was held in place with alignment pins and compressed with

ten bolts (5 N m torque) to ensure a homogeneous compression across the active area. After an initial conditioning with voltage steps described in previous works, polarization curves and limiting current measurements were conducted at 80 °C.³⁷ The polarization curves were recorded at a pressure of 150 kPa and gas humidity of 80% on the anode side and 60%/100% on the cathode side. H₂/air flow rates were set to 1.5 NL/min/3 NL/min. Galvanostatic steps of 25-100 mA cm⁻², lasting 30 s (≤ 200 mA cm⁻²)/3 min (> 200 mA cm⁻²), were set until the limit of 0.45 V was reached. For each data point in the presented curves, the voltage was averaged over the last third of the voltage step. The limiting current measurements were taken in both dry (60%/60%) and wet (80%/95%) conditions. 24 dilution levels of O₂ in N₂ were chosen from 1% to 100% oxygen. A vertical slope of the cell voltage was observed for dilution levels of at least up to 40% or higher, depending on the operating conditions. For the analysis, only dilution levels below 50% were chosen. Even though at higher oxygen concentration levels, the voltage slope at 50 mV indicated not only mass transfer limited current, the calculated oxygen transport resistances coalesce well with the observations and trends seen at lower oxygen levels. Prior to each measurement point, the oxygen level was set and a potential of 0.7 V held for ten minutes. Subsequently five potential steps from 0.3 V to 0.05 V were applied for 150 s each. Depending on the O₂ concentration (to prevent the influence of hydrogen evolution on the cathode side), a different voltage criterion was selected, following the procedure suggested and described in literature (0.15 V for xO₂ below 2%, 0.15 V between 3% - 8%, and 0.05 V for all higher dilution levels).³⁶ The oxygen transport resistance was then calculated with Equation 1.

$$R_T = \frac{4F}{R \cdot T_{cell}} \cdot \frac{(p_{abs} - p_{H_2O})}{i_{lim}} \cdot x_{O_2, dry} \quad (1)$$

5.3 Tomography Cell Assembly and Conditioning

Tomography cells with BMA5 graphite flow fields as described by Nagai et al. were used for all imaging experiments.⁹ First, the gasket (75 μm FEP, laser cut) was placed on a flow field. In the now 175 μm deep groove of the two-channel flow-field and gasket a GDL was carefully placed and the self-standing MPL placed on top. For the tomography cells, self-standing MPLs were used as precaution to have similar conditions at the CCM for both GDLs on the small active areas. With care, the laser cut CCM (fully catalyzed Gore Primea® (A510.1/M815.15/C510.4)) was now placed on top without removing or shifting GDL or MPL. The CCMs had an active area of 16 mm² (4.5 mm x 3.6 mm), that was fully illuminated during the scans by the X-ray beam. This ensured, that any degradation of the membrane would be monitored with the cell performance. The second flow-field, prepared as before, was then flipped onto the assembly, secured and compressed.

All cells were conditioned in the laboratory prior to exposure to X-rays during experiments at the beamline. After heating up the cell to 60 °C under N₂ flow (fully humidified on both sides) reactive gases were set to 100 NmL/min H₂ on anode and 79 NmL/min N₂ + 21 NmL/min O₂ on the cathode side at a dew-point of 60 °C. A voltage step cycle was then repeated for 10 times, following a similar procedure as described above.

5.4 Operando XTM Imaging

5.4.1 Operating Conditions

Two sets of experiments were conducted at the Tomcat beamline of the Swiss Light Source (SLS) at the Paul Scherrer Institut (PSI): potentio-static polarization curves at overly wet conditions (110% RH) to observe quasi steady-state water distributions in the fuel cell's GDL structure and a current jump with a set of fast scans to capture the water dynamics and the creation of the percolation network.

At the beamline, a highly developed setup was used in combination with a heated slip-ring

used to enable a continuous rotation of the cell while scanning.³⁸ The humidity was set with a custom-build Nafion-tube humidifier and the dewpoint was verified with a condensation mirror. Later, at the end of the scans, this was controlled with a dewpoint ramp while imaging the cells. When condensation was starting in the fuel cell’s channels, the 100 % RH value was determined and checked.

The cell was operated at 60 °C and initial polarization curves at full humidification as in the preparatory experiments where recorded to compare their performance. Prior to the current jump experiment, the cell was dried via blowing dry N₂ on both sides and the drying process observed with the rising HFR. An additional dry scan was acquired to confirm a dry structure. Contrary to prior to a polarization curve, the cell was initially dried but then operated for 5 min at the chosen experimental conditions and a cell potential of 700 mV. The operating conditions are summarized in Table 2.

Table 2: Summary of the operating conditions for all tomography cells during the XTM experiments.

Experiment	Gas Flow (A/C) [NmL/min]	Gas	Humidity (A/C) [%]	Duration [min]	Scans [-]
Pol. Curve	100/100	H ₂ /Air	110/110	3/step	39
Curr. Jump	100/100	H ₂ /Air	110/110	45 @ 0.8 A cm ⁻²	30

5.4.2 Imaging Conditions

XTM scans were acquired at the TOMCAT beamline with a 4-fold high efficiency microscope (Optique Peter, France) coupled with a GigaFRoST camera.³⁹ The power of the polychromatic beam from the synchrotron was filtered to 5 % (mean energy around 37 keV) and a 1 mm thick Si-wafer was used as an additional filter to reduce beam damage by hardening the beam and decreasing its flux.⁴⁰ All scans were performed with a voxel size of 2.75 μ m, an exposure time of 0.83 ms. All scans before and during the experiments were taken with 301 projections/180° to limit the total exposure time of the cells. The accumulated illumination time was kept just below 30 s. This time limit was found and reported to be safe to limit

beam damage to the cells at the used beam energy (5% white beam) and imaging conditions.⁴¹ High quality reference scans of each cell were taken at the end of the experiment series with 1201 projections/180°.

The polarization curve experiments were conducted at symmetric humidity of 110% under H₂/Air operation of the cells. After an initial drying in N₂, wet reactive gases were switched on and the cell potential was initially set to 700 mV for 5 min. The subsequent potential steps ranged from 900 mV to 300 mV in 50 mV steps of 3 min duration. A scan was taken every minute, summing up to a total number of 39 scans and a total illumination time of 9.7 s (cf. Figure S2). The three scans provided information of the water profile development during a step, but also granted backup data in case of a e.g. a shutter failure. Table 3 summarizes the used imaging parameters.

The current jump experiment started with an initial cell drying step as described before. Afterwards, reactive gases (H₂/Air) were switched on together with the load, that drew a constant current of 128 mA (corresponding to a current density of 0.8 A cm⁻²) for 25 min. During this time, 30 scans were conducted while the cell was continuously rotating. The scans were distributed nonuniformly with a higher density at the beginning to capture the water saturation development and later with more space to capture the "steady state" water distribution.

Table 3: Summary of the imaging conditions during *operando* experiments.

Experiment	Exposure time [ms]	Projections [-]	Scans [-]	Tot. Illumination [s]	Rotation [°]
Test scans	0.83	301	6	1.25	180
Pol. Curve	0.83	301	39	9.743	180
Curr. Jump	0.83	301	30	7.495	180
HQ-Reference Scan	0.83	1201	1	0.997	180

5.5 Data Processing

5.5.1 Reconstruction and Segmentation

The single tomograms were reconstructed (with Paganin phase retrieval) using the reconstruction pipeline available at TOMCAT.^{42,43} The high quality reference scan was then rotated rigidly with Fiji to orientate the cell with the cropped volume.⁴⁴ The low-quality reference scan and all other experimental scans were aligned using SimpleElastix to the previously rotated high quality reference scan. Difference images were created in the same tool by subtracting the dry, low-quality reference scan from the single wet images. All remaining data treatment was then performed in MATLAB 2019b/2020b.

The solid structure was gained from the reconstructed high-quality reference scan (cf. Figure S3). First, the flow field was segmented by applying a 5 px wide median kernel, determining the threshold value and subsequent thresholding (3×10^{-6}). The result was then multiplied with a mask of the GDL and channel areas (possible to determine due to the alignment in Fiji), leaving out only the flow field. With this, a region volume filter was applied, deleting all remaining islands consisting of less than 100 000 voxels. Three erode and three dilate operations to get rid of remaining GDL fiber pixels where then concluded with a hole-filling operation, to grant a solid structure of the flow-fields.

In the next step, the catalyst layer was segmented. Due to the high X-ray absorption of the Pt-particles therein no filtering was required and a simple thresholding (0.8×10^{-5}) was sufficient in combination with some island cleaning (omitting clusters smaller than 10 000 voxels).

As the last part of the solid segmentation, the GDL was segmented. First, an anisotropic diffusion filter (5 iterations) was applied and the threshold value determined (1.5×10^{-6}). Second, the image was binarized and multiplied with the inverted, segmented flow field and CCM, to obtain only GDL structures. After this, only one opening step was applied to smooth the fiber surface. As all fibers are connected with the binder in the used Toray

Paper, detached clusters of less than 500 voxels were omitted.

For the water segmentation the "dry", low-quality reference scan (identical imaging conditions as during the experiments) was subtracted from the aligned single "wet" scans acquired during the experiments. The resulting difference image was filtered with a non local means filter (density of states was chosen with 3×10^{-6}), thresholded (0.7×10^{-6}) and binarized. The binary operations to clean the data consisted only of an open and close step, finalized by neglecting all clusters smaller than 1000 voxels (i.e. <21 pL), neglecting only an insignificant amount of voxels classified as water.

5.5.2 Water Content Calculations

The water content of the GDL was calculated for an observation domain with the size of the CCM for both anode and cathode GDL separately. Along permuting axes, 2D and 1D saturation profiles along/across the channel and across the GDL height were calculated using the local void volume fraction from the segmented dry structure (from HQ scan) and the segmented water volume (from fast, LQ scans).

For the water cluster analysis of the perforated sample *T60-P5:100*, the observation volume (V) was further cropped to exclude slits located at the edges. Reference volumes were determined for each slit, as is shown in S7. For each time step, clusters with at least one voxel (vx) in this volume were labeled as "connected", the remaining water as "unconnected". By taking care of the scan order, also unconnected water clusters could be labeled as "previously connected", which was used for the cumulative cluster span analysis.

With these labels the saturation S_w , the connectivity C_w and an introduced bounding

box R_V span metric were calculated:

$$S_W = \frac{V_{H_2O}}{V_{tot}} = \frac{\sum vx_{H_2O}}{\sum vx_{void}} \quad (2)$$

$$C_W = \frac{V_{H_2O,conn.}}{V_{H_2O,tot}} = \frac{\sum vx_{H_2O,conn.}}{\sum vx_{H_2O,tot}} \quad (3)$$

$$R_V = \frac{V_{Rv}}{V_{tot}} = \frac{\sum vx_{Rv}}{\sum vx_{tot}} \quad (4)$$

For the metric R_V a bounding box was spanned across the stretches of connected water. This box volume was then set into relation to the total observed volume.

Acknowledgement

The authors thank the Swiss Federal Office of Energy for funding this project, Salvatore De Angelis and Mayank Sabharwal for support during the beamline campaign, Jens Eller for input and discussion for the beamline experiments and Thomas Gloor for the technical support. Finally, the provision of synchrotron radiation beamtime at the TOMCAT beamline of the Swiss Light Source (SLS) at the Paul Scherrer Institut, Switzerland, is gratefully acknowledged.

This project was funded under the grant SI/501635-01 from the Swiss Federal Office of Energy.

Supporting Information Available

The supporting information contains following further details:

- Performance data of the tomography fuel cells during the operando XTM experiments
- Segmentation details with separated, segmented solid phases
- Additional 1D and 2D saturation plots along different axes
- Details of the cropped cathode GDL area for water cluster calculations

References

- (1) Ball, M.; Weeda, M. The hydrogen economy - Vision or reality? *International Journal of Hydrogen Energy* **2015**, *40*, 7903–7919.
- (2) Stolten, D.; Samsun, R. C.; Garland, N. *Fuel cells: data, facts, and figures*; John Wiley & Sons, 2016.
- (3) Ajanovic, A.; Haas, R. Economic and Environmental Prospects for Battery Electric- and Fuel Cell Vehicles: A Review. *Fuel Cells* **2019**, *19*, 515–529.
- (4) Cano, Z. P.; Banham, D.; Ye, S.; Hintennach, A.; Lu, J.; Fowler, M.; Chen, Z. Batteries and fuel cells for emerging electric vehicle markets. *Nature Energy* **2018**, *3*, 279–289.
- (5) Suzuki, T.; Iiyama, A.; Kubo, N.; Saito, N.; Shinohara, K.; Shimotori, S.; Sugawara, Y.; Yamada, K. (Invited) Toward the Future Fuel Cell -Challenge for 2040-. *ECS Transactions* **2019**, *92*, 3–7.
- (6) Konno, N.; Mizuno, S.; Nakaji, H.; Ishikawa, Y. Development of Compact and High-Performance Fuel Cell Stack. *SAE International Journal of Alternative Powertrains* **2015**, *4*, 2015–01–1175.
- (7) Mathias, M. F.; Roth, J.; Fleming, J.; Lehnert, W. Diffusion media materials and characterisation. *Handbook of Fuel Cells* **2010**, *3*, 517–537.
- (8) Simon, C.; Kartouzian, D.; Müller, D.; Wilhelm, F.; Gasteiger, H. A. Impact of Microporous Layer Pore Properties on Liquid Water Transport in PEM Fuel Cells: Carbon Black Type and Perforation. *Journal of The Electrochemical Society* **2017**, *164*, F1697–F1711.
- (9) Nagai, Y.; Eller, J.; Hatanaka, T.; Yamaguchi, S.; Kato, S.; Kato, A.; Marone, F.; Xu, H.; Büchi, F. N. Improving water management in fuel cells through microporous

- layer modifications: Fast operando tomographic imaging of liquid water. *Journal of Power Sources* **2019**, *435*, 226809.
- (10) Lee, W. K.; Ho, C. H.; Van Zee, J. W.; Murthy, M. Effects of compression and gas diffusion layers on the performance of a PEM fuel cell. *Journal of Power Sources* **1999**, *84*, 45–51.
 - (11) Mench, M. M. In *Fuel Cell Engines*; Mench, M. M., Ed.; John Wiley & Sons, Inc.: Hoboken, NJ, USA, 2008; pp 1–515.
 - (12) Zenyuk, I. V.; Parkinson, D. Y.; Connolly, L. G.; Weber, A. Z. Gas-diffusion-layer structural properties under compression via X-ray tomography. *Journal of Power Sources* **2016**, *328*, 364–376.
 - (13) Holzer, L.; Pecho, O.; Schumacher, J.; Marmet, P.; Stenzel, O.; Büchi, F.; Lamibrac, A.; Münch, B. Microstructure-property relationships in a gas diffusion layer (GDL) for Polymer Electrolyte Fuel Cells, Part I: effect of compression and anisotropy of dry GDL. *Electrochimica Acta* **2017**, *227*, 419–434.
 - (14) Oberholzer, P.; Boillat, P. Local Characterization of PEFCs by Differential Cells: Systematic Variations of Current and Asymmetric Relative Humidity. *Journal of The Electrochemical Society* **2014**, *161*, F139–F152.
 - (15) Holzer, L.; Pecho, O.; Schumacher, J.; Marmet, P.; Büchi, F. N.; Lamibrac, A.; Münch, B. Microstructure-property relationships in a gas diffusion layer (GDL) for Polymer Electrolyte Fuel Cells, Part II: pressure-induced water injection and liquid permeability. *Electrochimica Acta* **2017**, *241*, 414–432.
 - (16) Niblett, D.; Mularczyk, A.; Niasar, V.; Eller, J.; Holmes, S. Two-phase flow dynamics in a gas diffusion layer - gas channel - microporous layer system. *Journal of Power Sources* **2020**, *471*, 228427.

- (17) Pasaogullari, U.; Wang, C. Y. Two-phase transport and the role of micro-porous layer in polymer electrolyte fuel cells. *Electrochimica Acta* **2004**, *49*, 4359–4369.
- (18) Eller, J.; Roth, J.; Marone, F.; Stampanoni, M.; Büchi, F. N. Operando Properties of Gas Diffusion Layers: Saturation and Liquid Permeability. *Journal of The Electrochemical Society* **2017**, *164*, F115–F126.
- (19) Mularczyk, A.; Lin, Q.; Blunt, M. J.; Lamibrac, A.; Marone, F.; Schmidt, T. J.; Büchi, F. N.; Eller, J. Droplet and Percolation Network Interactions in a Fuel Cell Gas Diffusion Layer. *Journal of The Electrochemical Society* **2020**, *167*, 084506.
- (20) Basu, S.; Wang, C.-Y.; Chen, K. S. Phase Change in a Polymer Electrolyte Fuel Cell. *Journal of The Electrochemical Society* **2009**, *156*, B748.
- (21) Baker, D. R.; Caulk, D. A.; Neyerlin, K. C.; Murphy, M. W. Measurement of Oxygen Transport Resistance in PEM Fuel Cells by Limiting Current Methods. *Journal of The Electrochemical Society* **2009**, *156*, B991.
- (22) Markötter, H.; Dittmann, K.; Haußmann, J.; Alink, R.; Gerteisen, D.; Riesemeier, H.; Scholta, J.; Banhart, J.; Manke, I. Influence of local carbon fibre orientation on the water transport in the gas diffusion layer of polymer electrolyte membrane fuel cells. *Electrochemistry Communications* **2015**, *51*, 133–136.
- (23) Liu, C. P.; Saha, P.; Huang, Y.; Shimpalee, S.; Satjaritanun, P.; Zenyuk, I. V. Measurement of Contact Angles at Carbon Fiber-Water-Air Triple-Phase Boundaries Inside Gas Diffusion Layers Using X-ray Computed Tomography. *ACS Applied Materials and Interfaces* **2021**, *13*, 20002–20013.
- (24) Koresawa, R.; Utaka, Y. Improvement of oxygen diffusion characteristic in gas diffusion layer with planar-distributed wettability for polymer electrolyte fuel cell. *Journal of Power Sources* **2014**, *271*, 16–24.

- (25) Forner-Cuenca, A.; Biesdorf, J.; Manzi-Orezzoli, V.; Gubler, L.; Schmidt, T. J.; Boillat, P. Advanced Water Management in PEFCs: Diffusion Layers with Patterned Wettability. *Journal of The Electrochemical Society* **2016**, *163*, F1389–F1398.
- (26) Forner-Cuenca, A.; Biesdorf, J.; Manzi-Orezzoli, V.; Gubler, L.; Schmidt, T. J.; Boillat, P. Advanced Water Management in PEFCs: Diffusion Layers with Patterned Wettability. *Journal of The Electrochemical Society* **2016**, *163*, F1389–F1398.
- (27) Gerteisen, D.; Heilmann, T.; Ziegler, C. Enhancing liquid water transport by laser perforation of a GDL in a PEM fuel cell. *Journal of Power Sources* **2008**, *177*, 348–354.
- (28) Gerteisen, D.; Sadeler, C. Stability and performance improvement of a polymer electrolyte membrane fuel cell stack by laser perforation of gas diffusion layers. *Journal of Power Sources* **2010**, *195*, 5252–5257.
- (29) Manahan, M. P.; Hatzell, M. C.; Kumbur, E. C.; Mench, M. M. Laser perforated fuel cell diffusion media. Part I: Related changes in performance and water content. *Journal of Power Sources* **2011**, *196*, 5573–5582.
- (30) Hussain, N.; Van Steen, E.; Tanaka, S.; Levecque, P. Metal based gas diffusion layers for enhanced fuel cell performance at high current densities. *Journal of Power Sources* **2017**, *337*, 18–24.
- (31) Alink, R.; Haußmann, J.; Markötter, H.; Schwager, M.; Manke, I.; Gerteisen, D. The influence of porous transport layer modifications on the water management in polymer electrolyte membrane fuel cells. *Journal of Power Sources* **2013**, *233*, 358–368.
- (32) Baker, D. R.; Caulk, D. A.; Neyerlin, K. C.; Murphy, M. W. Measurement of Oxygen Transport Resistance in PEM Fuel Cells by Limiting Current Methods. *Journal of The Electrochemical Society* **2009**, *156*, B991.

- (33) Parikh, N.; Allen, J. S.; Yassar, R. S. Microstructure of gas diffusion layers for PEM fuel cells. *Fuel Cells* **2012**, *12*, 382–390.
- (34) El-Kharouf, A.; Mason, T. J.; Brett, D. J.; Pollet, B. G. Ex-situ characterisation of gas diffusion layers for proton exchange membrane fuel cells. *Journal of Power Sources* **2012**, *218*, 393–404.
- (35) Ion, J. C. Laser processing of engineering materials : principles, procedure and industrial application . 2005.
- (36) Simon, C.; Hasché, F.; Gasteiger, H. A. Influence of the Gas Diffusion Layer Compression on the Oxygen Transport in PEM Fuel Cells at High Water Saturation Levels. *Journal of The Electrochemical Society* **2017**, *164*, F591–F599.
- (37) Csoklich, C.; Steim, R.; Marone, F.; Schmidt, T. J.; Büchi, F. N. Gas Diffusion Layers with Deterministic Structure for High Performance Polymer Electrolyte Fuel Cells. *ACS Applied Materials & Interfaces* **2021**, *13*, 9908–9918.
- (38) Xu, H.; Nagashima, S.; Nguyen, H. P.; Kishita, K.; Marone, F.; Büchi, F. N.; Eller, J. Temperature dependent water transport mechanism in gas diffusion layers revealed by subsecond operando X-ray tomographic microscopy. *Journal of Power Sources* **2021**, *490*, 229492.
- (39) Mokso, R.; Schlepütz, C. M.; Theidel, G.; Billich, H.; Schmid, E.; Celcer, T.; Mikuljan, G.; Sala, L.; Marone, F.; Schlumpf, N.; Stampanoni, M. GigaFRoST: The gigabit fast readout system for tomography. *Journal of Synchrotron Radiation* **2017**, *24*, 1250–1259.
- (40) Xu, H.; Marone, F.; Nagashima, S.; Nguyen, H.; Kishita, K.; Büchi, F. N.; Eller, J. (Invited) Exploring Sub-Second and Sub-Micron X-Ray Tomographic Imaging of Liquid Water in PEFC Gas Diffusion Layers. *ECS Transactions* **2019**, *92*, 11–21.

- (41) Eller, J.; Büchi, F. N. Polymer electrolyte fuel cell performance degradation at different synchrotron beam intensities. *Journal of Synchrotron Radiation* **2014**, *21*, 82–88.
- (42) Paganin, D.; Mayo, S. C.; Gureyev, T. E.; Miller, P. R.; Wilkins, S. W. Simultaneous phase and amplitude extraction from a single defocused image of a homogeneous object. *Journal of Microscopy* **2002**, *206*, 33–40.
- (43) Marone, F.; Studer, A.; Billich, H.; Sala, L.; Stampanoni, M. Towards on-the-fly data post-processing for real-time tomographic imaging at TOMCAT. *Advanced Structural and Chemical Imaging* **2017**, *3*, 1–11.
- (44) Schindelin, J.; Arganda-Carreras, I.; Frise, E.; Kaynig, V.; Longair, M.; Pietzsch, T.; Preibisch, S.; Rueden, C.; Saalfeld, S.; Schmid, B.; Tinevez, J. Y.; White, D. J.; Hartenstein, V.; Eliceiri, K.; Tomancak, P.; Cardona, A. Fiji: An open-source platform for biological-image analysis. *Nature Methods* **2012**, *9*, 676–682.

Graphical TOC Entry

Laser-perforated GDLs improve water transport and cell performance

